Received: 10 January 2024 | Revised: 10 April 2024 | Accepted: 30 June 2024

DOI: 10.1111/sapm.12740

STUDIES IN APPLIED MATHEMATICS WILEY

ORIGINAL ARTICLE

Steady Boussinesq convection: Parametric analyticity and computation

Jeremiah S. Lane | **Benjamin F. Akers**

Department of Mathematics, Air Force Institute of Technology, Ohio, USA

Correspondence
Jeremiah Lane, Department of Mathematics, Air Force Institute of Technology, 2950 Hobson Way, WPAFB, OH, USA.
Email: jeremiah.lane@afit.edu

Funding information
Air Force Office of Scientific Research

Abstract

Steady solutions to the Navier–Stokes equations with internal temperature forcing are considered. The equations are solved in two dimensions using the Boussinesq approximation to couple temperature and density fluctuations. A perturbative Stokes expansion is used to prove that that steady flow variables are parametrically analytic in the size of the forcing. The Stokes expansion is complemented with analytic continuation, via functional Padé approximation. The zeros of the denominator polynomials in the Padé approximants are observed to agree with a numerical prediction for the location of singularities of the steady flow solutions. The Padé representations not only prove to be good approximations to the true flow solutions for moderate intensity forcing, but are also used to initialize a Newton solver to compute large amplitude solutions. The composite procedure is used to compute steady flow solutions with forcing several orders of magnitude larger than the fixed-point method developed in previous work.

KEYWORDS
analytic continuation, convection, Navier–Stokes, Padé approximant, steady-state, Stokes expansion

1 | INTRODUCTION

The computation and analysis of steady solutions to the Navier–Stokes (NS) equations are challenging and important topics with many applications in engineering and physics. This work is concerned with natural convection, which has a vast accompanying literature describing efforts and applications in its simulation. Such applications undergoing active study include problems in gas turbine engine heat transfer,[1] the cooling of nuclear reactors,[2] the manipulation of fluids containing microparticles,[3,4] and nanoparticles,[5–8] and more recently, the simulation of laser beam propagation through a fluid medium.[9–11] In problems where natural convection dictates the fluid dynamics, the use of the Boussinesq approximation has been standard for decades.[12] In both steady and transient studies, there is a vast literature on the numerical methods used to simulate the Boussinesq equations for nonstandard geometries,[13] turbulent flow,[14,15] flow induced by temperature boundary conditions,[16] and with internal heat generation.[17] The numerical methods used to solve the transient problem have been thoroughly investigated,[18] but the simulation of steady-state problems for a general domain and forcing continue to present difficulties. The forced, steady NS equations are a nonlocal nonlinear system of partial differential equations, whose solutions are fixed points of the dynamic equations. For the steady problem with internal heat generation, previous efforts for numerical simulation have included fixed-point approaches with iteration over the fluid variables[19] as well as perturbative solutions in a parameter that measures the degree of heat transport in the flow.[20]

In this article, we show that the steady flow solutions to the NS equations (with Boussinesq approximation) are parametrically analytic in an intensity parameter, ε, that measures the size of the heating. This is achieved via a Stokes expansion of the fluid variables in ε, which works to decompose the fully coupled, nonlinear system into a sequence of linear systems, which can be solved recursively. This perturbative approach to the solutions of nonlinear PDEs is common in the analysis of nonlinear waves, in the computation of coherent structures in potential flow,[21–23] in weakly nonlinear models,[24–26] and in electromagnetic scattering problems[27,28] and the computation of the stability of these structures.[29–33] After proving parametric analyticity, steady solutions can be computed by direct evaluation of the perturbative expansion for ε within its radius of convergence. In order to compute steady solutions for higher intensity forcing, a functional Padé approximant of the solution is computed. The functional Padé approximant takes a formal power series representation of a function and generates a rational approximant to the function up to a specified order.[34] This method extends the range of ε for which solutions are computed.

Padé approximants have been exceedingly useful at providing an accurate approximation to the underlying function when outside the domain of convergence. Efforts over the past half decade have produced myriad results[35] with respect to row convergence properties in the Padé table,[36] Padé representation for finite-dimensional vector-valued functions,[37] and for generating functions that themselves have functional coefficients in their series representations.[35] Careful consideration of the computation of the Padé approximants must be taken due to the possible large size that the series coefficients may take. Nicholls and Reitich[38] show, for example, that the error in a Stokes expansion for traveling water waves may begin to grow past a certain number of terms due to floating point errors. An additional difficulty is due to the ill-conditioning of the linear system that may arise in the computation of the coefficients of the Padé approximant. Recent work by Gonnet, Güttel, and Trefethen[39] was aimed toward developing improved algorithms in classical Padé computation via a singular value decomposition (SVD) approach to increase algorithmic robustness against floating-point noise. The algorithm identifies and removes spurious pole-zero pairs called Froissart doublets,[40] which improves the approximation near the spurious poles and

clarifies which poles are likely to be genuine to the generating function. One advantage of the functional Padé approximation that we adopt in this article is a built-in spurious pole removal, which is accomplished by smoothing out the denominator polynomial via inner products. The remaining poles in the scalar denominator polynomial can then be used to estimate the location of singularities in the generating functions, which informs on the radius of convergence of the Stokes expansion of the steady fluid variables. While useful on its own, the Padé approximant may fail to accurately represent the true steady flow solutions when the intensity parameter becomes large. This motivates the use of a Padé–Newton method for high-intensity forcing where the functional Padé approximant is used as an initialization for Newton's method applied to a discretization of the steady Boussinesq system. Figure 8 toward the end of the article summarizes a diagram of the range of computable ε values for different numerical solvers in the steady Boussinesq problem.

The rest of the article is organized as follows. In Section 2, we introduce the system of equations to be solved, followed by the formulation of the perturbative Stokes expansion and computation of terms. Section 3 offers some results on the convergence of the Stokes expansion along with a proof of parametric analyticity in the intensity parameter ε. In Section 4, we describe the methodology and convergence properties of functional Padé approximation and a Padé–Newton method for finding high-intensity solutions. Section 5 is dedicated to an analysis of the poles in the Padé approximants, and Section 6 discusses the flow solutions for high-intensity forcing found through the Padé–Newton method.

2 | FORMULATION

We are interested in finding perturbative solutions to the 2D steady NS equations in the Boussinesq approximation with an internal temperature forcing term f,

$$(\mathbf{u}\cdot\nabla)T = \frac{1}{\mathrm{Pe}}\nabla^2 T + \varepsilon f, \tag{1a}$$

$$(\mathbf{u}\cdot\nabla)\omega = \frac{1}{\mathrm{Re}}\nabla^2\omega + \mathrm{Ri}\partial_x T, \tag{1b}$$

$$\nabla^2\psi = -\omega, \tag{1c}$$

where $u_1 = \partial_y\psi$ and $u_2 = -\partial_x\psi$. A square, bounded domain $\Omega \subset \mathbb{R}^2$ of length L is considered with homogeneous Dirichlet boundary conditions in stream function-vorticity variables. The parameters in the nondimensionalization (1) are the Reynolds (Re), Peclet (Pe), and Richardson (Ri) numbers common in convection, and the forcing f is normalized such that $\|f\| = 1$. In the simulation of laser propagation, for example, f is often a Gaussian centered in the middle of the domain Ω that represents the normalized laser intensity. The length scale of the problem, therefore, is taken to be the width w_0 of the forcing f, which is commonly the beam width of a Gaussian laser. We take $w_0 = 1$ cm for all results in the following sections and the domain length L is scaled by w_0 to be nondimensional. The parameter ε is then a measure of the intensity of the forcing. Formally expanding the variables T, ω, ψ in ε gives

$$T = \sum_{n=0}^{\infty}\varepsilon^n T_n, \quad \omega = \sum_{n=0}^{\infty}\varepsilon^n\omega_n, \quad \psi = \sum_{n=0}^{\infty}\varepsilon^n\psi_n, \tag{2}$$

where $T_0 = \omega_0 = \psi_0 = 0$. Substituting the series representation (2) into (1) and equating terms of equal order in ε gives a system of linear equations for each correction, whose first terms solve

$$\nabla^2 T_1 = -\mathrm{Pe} f, \tag{3a}$$

$$\nabla^2 \omega_1 = -\mathrm{RiRe}\partial_x T_1, \tag{3b}$$

$$\nabla^2 \psi_1 = -\omega_1, \tag{3c}$$

and whose general terms solve

$$\nabla^2 T_n = \mathrm{Pe}\left[\sum_{\ell=1}^{n-1} \partial_y \psi_\ell \partial_x T_{n-\ell} - \partial_x \psi_\ell \partial_y T_{n-\ell}\right], \tag{4a}$$

$$\nabla^2 \omega_n = \mathrm{Re}\left[\sum_{\ell=1}^{n-1} \partial_y \psi_\ell \partial_x \omega_{n-\ell} - \partial_x \psi_\ell \partial_y \omega_{n-\ell}\right] - \mathrm{RiRe}\partial_x T_n, \tag{4b}$$

$$\nabla^2 \psi_n = -\omega_n. \tag{4c}$$

Each correction (T_n, ω_n, ψ_n) can be computed using a linear Poisson equation solver up to a desired order $\mathcal{N}$, then an approximation to the full nonlinear solution is constructed by a finite truncation of the sums in Equation (2). We solve for the nth term with a finite-difference Poisson solver, where we enforce the boundary conditions on each term to satisfy a Navier-slip condition with zero temperature fluctuation on the boundary.

3 | CONVERGENCE RESULTS

The formal series developed above induces a numerical method, provided the series converges. Both ease of implementation and fast computation are advantages of this approach, where appropriate sparse solvers can be used as a fast Poisson solver in each term. We call this method the Stokes expansion or perturbation series for the remainder of the article. This section includes a formal proof that the series has a nonzero radius of convergence, as well as numerical observations of both the radius of convergence and the growth rates of the terms in the series. A numerical estimate for the radius of convergence is first established as a function of the nondimensional domain size L by observing the growth of terms in the Stokes expansion and comparing to a geometric series. We then apply rigorous analytical estimates to the size of these Stokes expansion terms to prove the parametric analyticity of the steady flow on the parameter ε.

3.1 | Radius of convergence estimate

A numerical estimate of the radius of convergence of the Stokes expansion can be found as follows. By plotting the 2-norm of terms against the index n for various domain sizes L, we observe that the growth rates of these series depend on domain size. Furthermore, the 2-norms of the corrections $\|T_n\|_2$ appear to grow or decay exponentially with n according to the general exponential

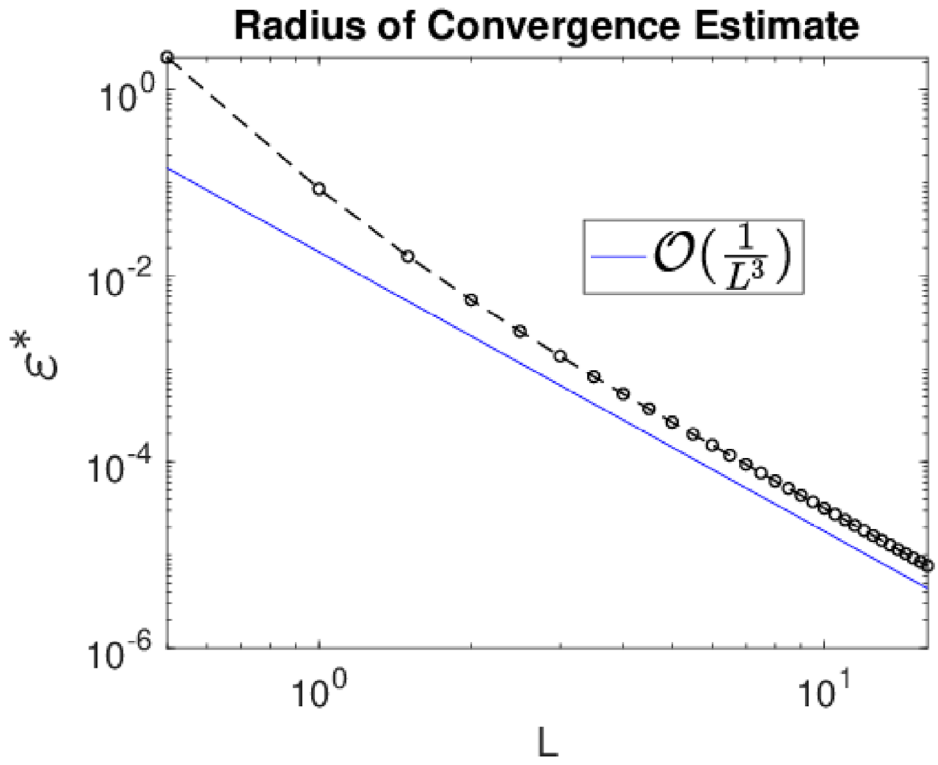

FIGURE 1 This figure depicts the estimate for the radius of convergence ε^* of the perturbation series as a function of the domain length along the dotted black line. This estimate has $O\left(\frac{1}{L^3}\right)$ asymptotic dependence with domain length, depicted according to the solid blue line.

relationship

$$\|T_n\|_2 = A\sigma^n, \tag{5}$$

for some exponential parameter $\sigma > 0$ that contains the domain size dependence. Via a comparison to the geometric series, the perturbation series (2) converges provided $\varepsilon < \frac{1}{\sigma}$. The exponential parameter σ is thus related to the radius of convergence ε^* by $\sigma = \frac{1}{\varepsilon^*}$. An estimate for the domain-dependent radius of convergence $\varepsilon^*(L)$ can then be established through determination of the exponential parameter $\sigma(L)$ through a least-squares fit according to its scaling with the temperature series terms (5). Figure 1 exhibits the estimate for the radius of convergence as a function of the domain length L.

At $L = 4$, the estimate for the radius of convergence is $\varepsilon^* \approx \frac{1}{1850}$ from the least squares determination of σ. To measure the convergence of the method in relation to this estimate, we track the error as a function of the number of terms in the series between the perturbation series approach and a convergent solution from a fixed-point method[19] at various ε values. We fix the domain size and discretization spacing to be $L = 4$ and $h = \frac{1}{16}$, respectively. Figure 2 shows the absolute error for $\varepsilon = \frac{1}{3000}$, $\varepsilon = \frac{1}{2000}$, and $\varepsilon = \frac{1}{1500}$.

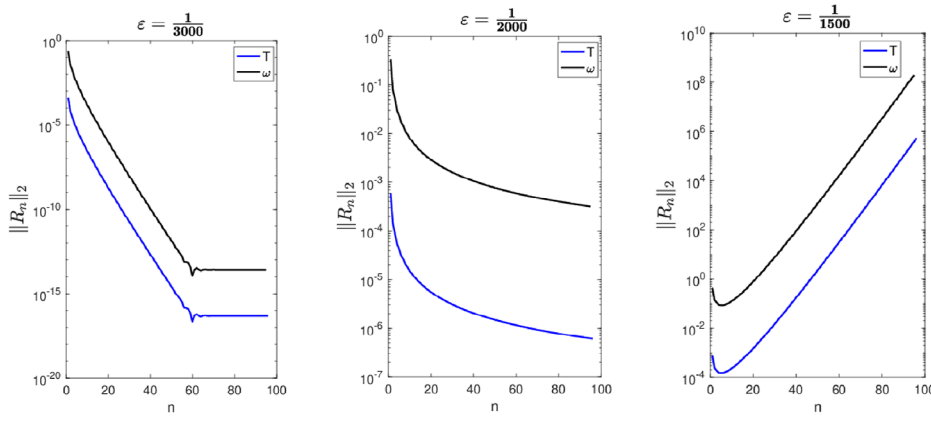

FIGURE 2 These panels exhibit the convergence properties of the perturbation series in the series remainder 2-norm $\|R_n\|_2$ determined from convergent fixed-point flow solutions T, ω for various ε values. Left: the series converges linearly for $\varepsilon = \frac{1}{3000}$. Middle: the series approaches sublinear convergence for $\varepsilon = \frac{1}{2000}$. Right: the series diverges for $\varepsilon = \frac{1}{1500}$.

For $\varepsilon = \frac{1}{3000}$ and $\varepsilon = \frac{1}{2000}$, we observe convergence, with the latter exhibiting a sublinear convergence rate. For $\varepsilon = \frac{1}{1500}$, however, the perturbation series diverges as the terms in the series grow too large. The effective radius of convergence thus acts as a limit on the intensity of forcing for which the perturbation series converges. For the same computational and fluid parameters, the fixed-point method in Ref. [19] converges for ε up to approximately $\frac{1}{1000}$. Hence, the direct summation of the perturbation series fails at lower laser intensities or absorption values compared to a fixed-point approach.

3.2 | Parametric analyticity

The numerical convergence of the perturbation series suggests that the steady flow variables may be parametrically analytic in the parameter ε within some convergence region $\mathcal{R} \subset \mathbb{C}$. Next, a proof of the parametric analyticity of the solution is presented, using the methodology developed for the water wave problem in Refs. [21, 24, 32].

The size of the $n = 1$ perturbations can be calculated by applying a classic estimate for solutions to Poisson's equation[41] to Equation (3) yielding

$$\|T_1\|_{H^2(\Omega)} \leq C\mathrm{Pe}\|f\|_{L^2(\Omega)}, \tag{6a}$$

$$\|\omega_1\|_{H^2(\Omega)} \leq C^2\mathrm{RiRePe}\|f\|_{L^2(\Omega)}, \tag{6b}$$

$$\|\psi_1\|_{H^2(\Omega)} \leq C^3\mathrm{RiRePe}\|f\|_{L^2(\Omega)}. \tag{6c}$$

Next, the functions $\mathcal{T}_n$ and $\mathcal{W}_n$ are defined to be the right-hand side of the expressions for the nth perturbation in T and ω, respectively,

$$\mathcal{T}_n = \mathrm{Pe}\left[\partial_y\psi_1\partial_x T_{n-1} - \partial_x\psi_1\partial_y T_{n-1} + \partial_y\psi_{n-1}\partial_x T_1 - \partial_x\psi_{n-1}\partial_y T_1 + \sum_{\ell=2}^{n-2}\left(\partial_y\psi_\ell\partial_x T_{n-\ell} - \partial_x\psi_\ell\partial_y T_{n-\ell}\right)\right], \tag{7}$$

$$\mathcal{W}_n = \mathrm{Re}\left[-\mathrm{Ri}\partial_x T_n + \partial_y\psi_1\partial_x\omega_{n-1} - \partial_x\psi_1\partial_y\omega_{n-1} + \partial_y\psi_{n-1}\partial_x\omega_1 - \partial_x\psi_{n-1}\partial_y\omega_1 + \sum_{\ell=2}^{n-2}\left(\partial_y\psi_\ell\partial_x\omega_{n-\ell} - \partial_x\psi_\ell\partial_y\omega_{n-\ell}\right)\right], \tag{8}$$

where the sum is set equal to zero for $n \leq 3$. To estimate the size of the corrections for large n, the following lemma is used to bound the right-hand sides, (7) and (8), in terms of the previous corrections. We proceed by introducing a positive constant D that relates the bounds on the size of corrections to the size of the functions $\mathcal{T}_n$ and $\mathcal{W}_n$.

Lemma 1 (Recursive Estimate). *Let $N \geq 3$ and let C be the positive constant from the elliptic estimate (6). For a large enough positive constant D, if each*

$$\|T_n\|_{H^2(\Omega)} \leq \widetilde{C}_T\frac{D^{n-2}}{(n+1)^2}, \quad 2 \leq n \leq N-1,$$

$$\|\omega_n\|_{H^2(\Omega)} \leq \widetilde{C}_\omega\frac{D^{n-2}}{(n+1)^2}, \quad 2 \leq n \leq N-1,$$

then

$$\|\mathcal{T}_N\|_{L^2(\Omega)} \leq \widetilde{C}_T C\frac{D^{N-3}}{(N+1)^2},$$

$$\|\mathcal{W}_N\|_{L^2(\Omega)} \leq \widetilde{C}_\omega C\frac{D^{N-3}}{(N+1)^2},$$

for some positive constants $\widetilde{C}_T$ and $\widetilde{C}_\omega$.

Proof. First, the elliptic estimate from (6) gives that

$$\|\psi_\ell\|_{H^2(\Omega)} \leq C\|\omega_\ell\|_{L^2(\Omega)} \leq C\|\omega_\ell\|_{H^2(\Omega)} \leq CC_\omega\frac{D^{n-2}}{(n+1)^2}.$$

Next, from the definition of $\mathcal{T}_N$ and from the fact that $H^2(\Omega)$ is an algebra[42]:

$$\|\mathcal{T}_N\|_{L^2(\Omega)} \leq \mathrm{Pe}\left[\sum_{\ell=2}^{N-2}\left(\|\partial_x\psi_\ell\partial_y T_{N-\ell}\|_{L^2(\Omega)} + \|\partial_y\psi_\ell\partial_x T_{N-\ell}\|_{L^2(\Omega)}\right) + \|\partial_y\psi_1\partial_x T_{N-1}\|_{L^2(\Omega)} + \|\partial_x\psi_1\partial_y T_{N-1}\|_{L^2(\Omega)} + \|\partial_y\psi_{N-1}\partial_x T_1\|_{L^2(\Omega)} + \|\partial_x\psi_{N-1}\partial_y T_1\|_{L^2(\Omega)}\right]$$

$$\leq 2\mathrm{Pe}\left[\sum_{\ell=2}^{N-2}\left(\|\psi_\ell T_{N-\ell}\|_{H^2(\Omega)}\right)+\|\psi_1 T_{N-1}\|_{H^2(\Omega)}+\|\psi_{N-1}T_1\|_{H^2(\Omega)}\right]$$

$$\leq 2M\mathrm{Pe}\left[\sum_{\ell=2}^{N-2}\left(\|\psi_\ell\|_{H^2(\Omega)}\|T_{N-\ell}\|_{H^2(\Omega)}\right)+\|\psi_1\|_{H^2(\Omega)}\|T_{N-1}\|_{H^2(\Omega)}+\|\psi_{N-1}\|_{H^2(\Omega)}\|T_1\|_{H^2(\Omega)}\right]$$

$$\leq 2M\mathrm{Pe}\left[\sum_{\ell=2}^{N-2}\left(CC_\omega\frac{D^{\ell-2}}{(\ell+1)^2}C_T\frac{D^{N-\ell-2}}{(N-\ell+1)^2}\right)+\frac{D^{N-3}}{N^2}(C^3C_T\mathrm{RiRePe}+C^2C_\omega\mathrm{Pe})\right]$$

$$=2MCC_\omega C_T\mathrm{Pe}\sum_{\ell=2}^{N-2}\left(\frac{D^{N-4}}{(\ell+1)^2(N-\ell+1)^2}\right)+2M\mathrm{Pe}\frac{D^{N-3}}{N^2}(C^3C_T\mathrm{RiRePe}+C^2C_\omega\mathrm{Pe})$$

$$=2MCC_\omega C_T\mathrm{Pe}\frac{D^{N-4}}{(N+1)^2}\sum_{\ell=2}^{N-2}\frac{(N+1)^2}{(\ell+1)^2(N-\ell+1)^2}$$

$$+2M\mathrm{Pe}\frac{D^{N-3}}{N^2}(C^3C_T\mathrm{RiRePe}+C^2C_\omega\mathrm{Pe}),$$

where M is a positive constant. Next the below sum,

$$S_N=\sum_{\ell=2}^{N-2}\frac{(N+1)^2}{(\ell+1)^2(N-\ell+1)^2},$$

is bounded for $N\geq 4$. First when N is odd, using the symmetry of the denominator,

$$\sum_{\ell=2}^{N-2}\frac{(N+1)^2}{(\ell+1)^2(N-\ell+1)^2}=2\sum_{\ell=2}^{\frac{N-1}{2}}\frac{(N+1)^2}{(\ell+1)^2(N-\ell+1)^2}.$$

Decomposing the sum into partial fractions yields

$$S_N=2\sum_{\ell=2}^{\frac{N-1}{2}}\frac{\ell^2}{(\ell+1)^2(N-\ell+1)^2}+\frac{2\ell}{(\ell+1)^2(N-\ell+1)}+\frac{1}{(\ell+1)^2}$$

$$=2\sum_{\ell=2}^{\frac{N-1}{2}}\frac{1}{(\ell+1)^2}\left(\frac{\ell^2}{(N-\ell+1)^2}+\frac{2\ell}{N-\ell+1}+1\right).$$

Since $\ell\leq\frac{N}{2}$,

$$\frac{\ell^2}{(N-\ell+1)^2}+\frac{2\ell}{N-\ell+1}+1\leq 4,$$

so

$$S_N\leq 8\sum_{\ell=2}^{\frac{N-1}{2}}\frac{1}{(\ell+1)^2}\leq 8\left(\frac{\pi^2}{6}-\frac{5}{4}\right)=S.$$

The same bound applies for N even, with similar proof, giving the updated bound

$$\|\mathcal{T}_N\|_{L^2(\Omega)} \leq 2MCC_\omega C_T S\mathrm{Pe}\frac{D^{N-4}}{(N+1)^2} + 2M\mathrm{Pe}\frac{D^{N-3}}{N^2}\left(C^3C_T\mathrm{RiRePe} + C^2C_\omega\mathrm{Pe}\right),$$

which satisfies the lemma for $D > \frac{25}{16}$, since $\frac{(N+1)^2}{DN^2} < 1$ for $N \geq 4$ and

$$\widetilde{C}_T = 2MC_\omega C_T S\mathrm{Pe} + 2M\mathrm{Pe}\left(C^2C_T\mathrm{RiRePe} + CC_\omega\mathrm{Pe}\right).$$

The bound on $\mathcal{W}_N$ follows a similar pattern, where

$$\begin{aligned}
\|\mathcal{W}_N\|_{L^2(\Omega)} &\leq \mathrm{Re}\left[\sum_{\ell=2}^{N-2}\left(\|\partial_x\psi_\ell\partial_y\omega_{N-\ell}\|_{L^2(\Omega)} + \|\partial_y\psi_\ell\partial_x\omega_{N-\ell}\|_{L^2(\Omega)}\right)\right.\\
&\quad\left.+\|\partial_y\psi_1\partial_x\omega_{N-1}\|_{L^2(\Omega)} + \|\partial_x\psi_1\partial_y\omega_{N-1}\|_{L^2(\Omega)} + \|\partial_y\psi_{N-1}\partial_x\omega_1\|_{L^2(\Omega)} + \|\partial_x\psi_{N-1}\partial_y\omega_1\|_{L^2(\Omega)}\right]\\
&\quad + \mathrm{ReRi}\|\partial_x T_N\|_{L^2(\Omega)}\\
&\leq 2\mathrm{Re}\left[\sum_{\ell=2}^{N-2}\left(\|\psi_\ell\omega_{N-\ell}\|_{H^2(\Omega)}\right) + \|\psi_1\omega_{N-1}\|_{H^2(\Omega)} + \|\psi_{N-1}\omega_1\|_{H^2(\Omega)}\right] + \mathrm{ReRi}\|T_N\|_{H^2(\Omega)}\\
&\leq 2M\mathrm{Re}\left[\sum_{\ell=2}^{N-2}\left(\|\psi_\ell\|_{H^2(\Omega)}\|\omega_{N-\ell}\|_{H^2(\Omega)}\right) + \|\psi_1\|_{H^2(\Omega)}\|\omega_{N-1}\|_{H^2(\Omega)} + \|\psi_{N-1}\|_{H^2(\Omega)}\|\omega_1\|_{H^2(\Omega)}\right]\\
&\quad + C\mathrm{ReRi}\|\mathcal{T}_N\|_{L^2(\Omega)}\\
&\leq 2M\mathrm{Re}\left[\sum_{\ell=2}^{N-2}\left(CC_\omega\frac{D^{\ell-2}}{(\ell+1)^2}C_\omega\frac{D^{N-\ell-2}}{(N-\ell+1)^2}\right) + \frac{D^{N-3}}{N^2}(2C^3C_\omega\mathrm{RiRePe})\right]\\
&\quad + C\mathrm{ReRi}\|\mathcal{T}_N\|_{L^2(\Omega)}\\
&= 2MCC_\omega^2\mathrm{Re}\sum_{\ell=2}^{N-2}\left(\frac{D^{N-4}}{(\ell+1)^2(N-\ell+1)^2}\right) + 2M\mathrm{Re}\frac{D^{N-3}}{N^2}(2C^3C_\omega\mathrm{RiRePe})\\
&\quad + C\mathrm{ReRi}\|\mathcal{T}_N\|_{L^2(\Omega)}\\
&= 2MCC_\omega^2\mathrm{Re}S\frac{D^{N-4}}{(N+1)^2} + 2M\mathrm{Re}\frac{D^{N-3}}{N^2}(2C^3C_\omega\mathrm{RiRePe}) + C\mathrm{ReRi}C_T\widetilde{C}\frac{D^{N-3}}{(N+1)^2}.
\end{aligned}$$

This satisfies the lemma for

$$\widetilde{C}_\omega = 2MC_\omega^2\mathrm{Re}S + 4MC^2C_\omega\mathrm{RiRe}^2\mathrm{Pe} + \mathrm{ReRi}C_T\widetilde{C}_T.$$

□

The following lemma bounds the size of each perturbation term.

Lemma 2 (Size of Perturbation Terms). *For $n \geq 2$, some constants C_T, C_ω, and $D > \max\left(\frac{25}{16}, C^2\frac{\tilde{C}_T}{C_T}, C^2\frac{\tilde{C}_\omega}{C_\omega}\right)$,*

$$\|T_n\|_{H^2(\Omega)} \leq C_T\frac{D^{n-2}}{(n+1)^2}, \quad \|\omega_n\|_{H^2(\Omega)} \leq C_\omega\frac{D^{n-2}}{(n+1)^2}, \quad \|\psi_n\|_{H^2(\Omega)} \leq CC_\omega\frac{D^{n-2}}{(n+1)^2}.$$

Proof. We proceed by strong induction. For the base $n = 2$ case, it suffices to pick the constants C_T, C_ω large enough to satisfy the hypothesis. Assuming the hypothesis holds for all $n < N$, $N \geq 3$, we apply an elliptic estimate and Lemma 1 to estimate

$$\|T_N\|_{H^2(\Omega)} \leq C\|\mathcal{T}_N\|_{L^2(\Omega)} \leq \widetilde{C}_T C^2\frac{D^{N-3}}{(N+1)^2},$$

$$\|\omega_N\|_{H^2(\Omega)} \leq C\|\mathcal{W}_N\|_{L^2(\Omega)} \leq \widetilde{C}_\omega C^2\frac{D^{N-3}}{(N+1)^2},$$

$$\|\psi_N\|_{H^2(\Omega)} \leq C\|\omega_N\|_{H^2(\Omega)} \leq \widetilde{C}_\omega C^3\frac{D^{N-3}}{(N+1)^2}.$$

For the hypothesis to hold for $\|T_N\|_{H^2(\Omega)}$, we require

$$\widetilde{C}_T C^2\frac{D^{N-3}}{(N+1)^2} \leq C_T\frac{D^{N-2}}{(N+1)^2},$$

which holds for

$$D > C^2\frac{\widetilde{C}_T}{C_T}.$$

Similarly, for the $\|T_N\|_{H^2(\Omega)}$ estimate, we require

$$\widetilde{C}_\omega C^2\frac{D^{N-3}}{(N+1)^2} \leq C_\omega\frac{D^{N-2}}{(N+1)^2},$$

which holds for

$$D > C^2\frac{\widetilde{C}_\omega}{C_\omega},$$

and for the $\|\psi_N\|_{H^2(\Omega)}$, we require

$$\widetilde{C}_\omega C^3\frac{D^{N-3}}{(N+1)^2} \leq CC_\omega\frac{D^{N-2}}{(N+1)^2},$$

which holds for the same D as above. Thus, for D satisfying the strict lower bounds, the lemma is satisfied. □

Next, the above lemmas are used to prove analyticity of the Stokes' expansion.

Theorem 1 (Parametric Analyticity of Steady Flow Variables). *The functions $T(x, y; \varepsilon) \in H^2(\Omega)$, $\omega(x, y; \varepsilon) \in H^2(\Omega)$, $\psi(x, y; \varepsilon) \in H^2(\Omega)$, which are solutions to the steady Boussinesq equations with*

homogeneous Dirichlet boundary conditions (1) are parametrically analytic in the parameter $\varepsilon \in \mathbb{C}$ for some $|\varepsilon| > 0$. That is, the series given by (2) converges for small enough $|\varepsilon|$.

Proof. Suppose that $|\varepsilon| < \frac{\rho}{D}$ for some $0 \leq \rho < 1$. The terms T_n in the perturbation series (2) are bounded by a p-series

$$|\varepsilon|^n \|T_n\|_{H^2(\Omega)} \leq |\varepsilon|^n C_T \frac{D^{n-2}}{(n+1)^2} = \frac{C_T}{D^2} \frac{\rho^n}{(n+1)^2}$$
$$\leq \frac{C_T}{D^2} \frac{1}{(n+1)^2}.$$

Since the p-series converges, so does the perturbation series

$$\left\| \sum_{n=1}^{\infty} \varepsilon^n T_n \right\|_{H^2(\Omega)} \leq \sum_{n=1}^{\infty} \frac{C_T}{D^2} \frac{1}{(n+1)^2}.$$

The result for ω_n and ψ_n follows similarly. □

Corollary 1 (Radius of Convergence Scaling). *The radius of convergence ε^* of the perturbation series (2) scales as* $\frac{1}{\varepsilon^*} = \mathcal{O}(\mathrm{Re\ Ri\ Pe} \max(\mathrm{Re}, \mathrm{Pe}))$.

Proof. From Theorem 1, the radius of convergence can be determined through $\frac{1}{\varepsilon^*} = D$. From Lemma 2, D satisfies $D \gtrsim \widetilde{C}_T$ and $D \gtrsim \widetilde{C}_\omega$. Lemma 1 then provides the scaling $\widetilde{C}_T = \mathcal{O}(\mathrm{Re\ Ri\ Pe}^2)$ and $\widetilde{C}_\omega = \mathcal{O}(\mathrm{Re}^2\ \mathrm{Ri\ Pe})$, so $\frac{1}{\varepsilon^*} = D = \mathcal{O}(\mathrm{Re\ Ri\ Pe} \max(\mathrm{Re}, \mathrm{Pe}))$. □

The radius of convergence for the Stokes expansion follows the same scaling as the effective radius for the convergence of the fixed-point method published in Ref. [19] as a function of the nondimensional Re, Ri, Pe numbers. The utility of both methods is therefore limited by the size of the intrinsic fluid parameters and by the computational domain size, as described in Figure 1. Each result can be thought of as a respective scaling in the two length scales of the problem: the spatial extent of the forcing w_0 that dictates the intrinsic flow parameters and the domain length L.

4 | ANALYTIC CONTINUATION

In some practical applications, such as the simulation of atmospheric laser propagation, the large ε regime is of interest.[43] Analytic continuation is a classic approach for using a perturbation series for large parameter values,[44] wherein the perturbation expansion is supplemented via Padé approximation.

4.1 | Functional Padé approximation

Padé approximation can be used to represent a divergent power series with a (potentially convergent) sequence of rational functions near singularities—locations where a polynomial cannot sufficiently approximate the underlying function. Padé approximation has proven to be an

incredibly powerful tool in approximation theory, even though many unanswered questions still remain with respect to the full extent of the effectiveness of the method.[44]

While Padé approximation is traditionally utilized for approximating power series with scalar coefficients in $\mathbb{R}$ or $\mathbb{C}$, the method may be generalized for series with coefficients in a vector space. This generalization is called vector Padé approximation or functional Padé approximation for coefficients in a function space.[35,37,45] A function $T \in H^2(\Omega)$ is represented by a rational function in the parameter ε with functional numerator coefficients and scalar denominator coefficients:

$$T(x,y;\varepsilon) \approx r^{[N/2k]}(x,y;\varepsilon) = \frac{p(x,y;\varepsilon)}{q(\varepsilon)} = \frac{p_0(x,y) + \varepsilon p_1(x,y) + \cdots + \varepsilon^N p_N(x,y)}{q_0 + \varepsilon q_1 + \cdots + \varepsilon^{2k} q_{2k}}. \tag{9}$$

There are several ways to construct this rational approximation, each depending on the axioms and desired properties of the representation. These include integral Padé approximants, hybrid Padé approximants, modified Padé approximants, and the method utilized in this work, functional Padé approximants.[45] For a function T with terms T_i in a formal power series in the parameter $\varepsilon \in \mathbb{C}$, the functional Padé approximant takes the form

$$r^{[n/2k]}(x,y;\varepsilon) = \frac{p(x,y;\varepsilon)}{q(\varepsilon)}, \tag{10}$$

where $r^{[n/2k]}(x,y;\varepsilon)$ denotes a rational function in ε of numerator degree n and denominator degree $2k$. The functions p and q are polynomials in the parameter ε that satisfy the following axioms[45]:

$$\deg(p) \leq n, \quad \deg(q) = 2k, \tag{11a}$$

$$q \Big| \langle p, p \rangle_{H^2(\Omega)}, \tag{11b}$$

$$T(x,y;\varepsilon) - r^{[n/2k]}(x,y;\varepsilon) = \mathcal{O}(\varepsilon^{n+1}), \tag{11c}$$

$$q(0) \neq 0. \tag{11d}$$

Condition (11a) specifies the degree of the polynomials p and q and condition (11b) enforces the divisibility of the polynomial $\langle p, p \rangle_{H^2(\Omega)}$ by the polynomial q, where $\langle \cdot, \cdot \rangle_{H^2(\Omega)}$ denotes the inner product in the $H^2(\Omega)$ space. These axioms ensure existence and uniqueness of the functional Padé approximant.[36]

Work by Baker and Graves–Morris[37,46] treats questions about existence, uniqueness, degeneracy, and construction of vector Padé approximants in the finite-dimensional case. The results, however, generalize naturally to approximants with numerator polynomials that exist in an infinite-dimensional function space. The most relevant result to our analysis is that functional Padé approximants satisfying the above axioms (11) are unique, and the denominator polynomial

may be constructed through a determinant formula[34]:

$$q(\varepsilon) = \begin{vmatrix} 0 & \mathcal{M}_{0,1} & \mathcal{M}_{0,2} & \dots & \mathcal{M}_{0,2k} \\ -\mathcal{M}_{0,1} & 0 & \mathcal{M}_{1,2} & \dots & \mathcal{M}_{1,2k} \\ \vdots & \vdots & \vdots & \vdots & \vdots \\ -\mathcal{M}_{0,2k-1} & -\mathcal{M}_{1,2k-1} & -\mathcal{M}_{2,2k-1} & \dots & \mathcal{M}_{2k-1,2k} \\ \varepsilon^{2k} & \varepsilon^{2k-1} & \varepsilon^{2k-2} & \dots & 1 \end{vmatrix}, \tag{12}$$

where $\mathcal{M}$ is a $(2k+1)\times(2k+1)$ matrix that satisfies the linear system

$$\mathcal{M}\mathbf{q} = \mathbf{0} \quad \text{for} \quad \mathbf{q} = [q_0, q_1, \dots, q_{2k}]^T. \tag{13}$$

Since $\mathcal{M}$ is a skew-symmetric matrix of odd order, a nontrivial solution to (13) exists. The elements of $\mathcal{M}$ are defined by

$$\mathcal{M}_{ij} = \sum_{\ell=0}^{j-i-1} \left\langle T_{\ell+i+n-2k+1}, T_{j-\ell+n-2k} \right\rangle_{H^2(\Omega)}, \tag{14}$$

where the inner product in the $H^2(\Omega)$ space is defined by

$$\left\langle u, v \right\rangle_{H^2(\Omega)} = \int_\Omega uv + \partial_x u \partial_x v + \partial_y u \partial_y v + \partial_{xx} u \partial_{xx} v + \partial_{xy} u \partial_{xy} v + \partial_{yy} u \partial_{yy} v \, d\Omega. \tag{15}$$

After the denominator polynomial is determined, the numerator polynomial $p(x, y; \varepsilon)$ is found through application of axiom (11c),

$$p(x, y; \varepsilon) = [q(\varepsilon) T(x, y; \varepsilon)]_0^n, \tag{16}$$

where the brackets in Equation (16) notate the partial sum of series coefficients such that

$$[T(x, y; \varepsilon)]_0^n = \sum_{i=0}^{n} \varepsilon^i T_i(x, y; \varepsilon) \tag{17}$$

for some T with series terms T_i.

In this work, each of the perturbation terms T_n, ω_n, ψ_n, were computed on a uniform Cartesian grid. Second-order finite difference approximations were used for the derivatives and the quadrature was performed with the trapezoidal rule. The numerator polynomial terms in the rational approximation will each be vectors with m^2 terms, where m^2 is the total number of points in the discretization over an $m \times m$ grid. We find the denominator polynomial q by interpreting (13) as an eigenvalue problem and computing the SVD of the matrix $\mathcal{M}$. The null vector associated with the smallest singular value is chosen for $\mathbf{q}$ where $\|\mathbf{q}\| = 1$ in the vector 2-norm. A similar SVD approach for noisy data was first introduced for classical Padé approximants by Gonnet et al.[39]

4.2 | Newton iteration

When the intensity parameter ε is large, the functional Padé approximant may fail to represent the steady flow solutions to a tolerable degree when high accuracy is required, for example, in

a simulation for laser propagation. In this case, the approximant may, however, still serve as a suitable initial guess for a Newton iteration. In this section, the Newton iteration for the 2D steady Boussinesq equations (1) is presented. The steady solutions solve $\mathcal{F}(T, \psi, \omega) = 0$, with

$$\mathcal{F}_1 = -(\mathbf{u} \cdot \nabla)T + \frac{1}{\mathrm{Pe}}\nabla^2 T + \varepsilon f, \tag{18a}$$

$$\mathcal{F}_2 = -(\mathbf{u} \cdot \nabla)\omega + \frac{1}{\mathrm{Re}}\nabla^2 \omega + \mathrm{Ri}\partial_x T, \tag{18b}$$

$$\mathcal{F}_3 = \nabla^2 \psi + \omega, \tag{18c}$$

with $u_1 = \psi_y$, and $u_2 = -\psi_x$. The generalized Newton iteration takes the following form for $n \geq 0$,

$$X_{n+1} = X_n - [D\mathcal{F}(X_n)]^{-1} F(X_n), \tag{19}$$

where the $X_0 = (T_0, \omega_0, \psi_0)$ initialization comes from the functional Padé approximant and $D\mathcal{F}(X_n)$ is the collection of partial Fréchet derivatives $D_T\mathcal{F}(X_n)$, $D_\omega\mathcal{F}(X_n)$, $D_\psi\mathcal{F}(X_n)$ of $\mathcal{F}$ at X_n. Each of the partial Fréchet derivatives are given below,

$$D_T f_1(X_n) = -\partial_y \psi_n \partial_x + \partial_x \psi_n \partial_y + \frac{1}{\mathrm{Pe}}\nabla^2, \tag{20a}$$

$$D_\omega f_1(X_n) = 0, \tag{20b}$$

$$D_\psi f_1(X_n) = \partial_y T_n \partial_x - \partial_x T_n \partial_y, \tag{20c}$$

$$D_T f_2(X_n) = \mathrm{Ri}\partial_x, \tag{20d}$$

$$D_\omega f_2(X_n) = -\partial_y \psi_n \partial_x + \partial_x \psi_n \partial_y + \frac{1}{\mathrm{Re}}\nabla^2, \tag{20e}$$

$$D_\psi f_2(X_n) = \partial_y \omega_n \partial_x - \partial_x \omega_n \partial_y, \tag{20f}$$

$$D_T f_3(X_n) = 0, \tag{20g}$$

$$D_\omega f_3(X_n) = \mathcal{I}, \tag{20h}$$

$$D_\psi f_3(X_n) = \nabla^2, \tag{20i}$$

where $\mathcal{I}$ is the identity operator. At this stage, each of the partial Fréchet derivatives can be discretized and the iteration (19) transformed to solve a system of algebraic equations at each point on the 2D grid,

$$\mathbf{X}_{n+1} = \mathbf{X}_n - J(\mathcal{F}(\mathbf{X}_n))^{-1}\mathcal{F}(\mathbf{X}_n), \tag{21}$$

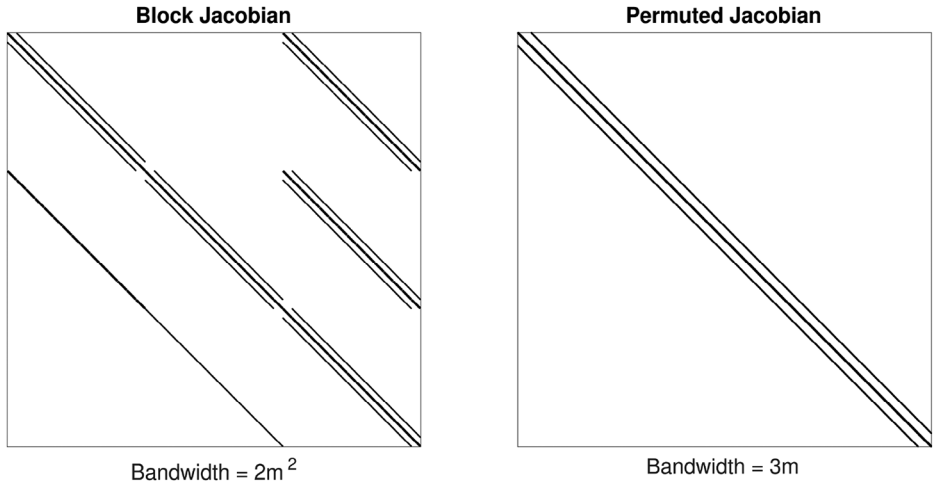

FIGURE 3 Left: Jacobian sparsity pattern as directly constructed from (22) with a bandwidth of 2 m^2 following discretization on an $m \times m$ grid. Right: Jacobian sparsity pattern following permutation to reduce bandwidth to 3 m.

where the collection of partial Fréchet derivatives becomes the Jacobian that may be constructed through the block matrix of discretized Fréchet derivatives

$$J = \begin{bmatrix} \mathbf{D}_T \mathcal{F}_1(\mathbf{X}_n) & \mathbf{D}_\omega \mathcal{F}_1(\mathbf{X}_n) & \mathbf{D}_\psi \mathcal{F}_1(\mathbf{X}_n) \\ \mathbf{D}_T \mathcal{F}_2(\mathbf{X}_n) & \mathbf{D}_\omega \mathcal{F}_2(\mathbf{X}_n) & \mathbf{D}_\psi \mathcal{F}_2(\mathbf{X}_n) \\ \mathbf{D}_T \mathcal{F}_3(\mathbf{X}_n) & \mathbf{D}_\omega \mathcal{F}_3(\mathbf{X}_n) & \mathbf{D}_\psi \mathcal{F}_3(\mathbf{X}_n) \end{bmatrix}. \tag{22}$$

Due to the size of the Jacobian and the sparsity of each of the block matrix elements, it is beneficial to minimize its bandwidth to improve computational performance in a sparse linear solver. This may be achieved by alternating the appropriate rows and columns in the direct construction of the Jacobian. Alternatively, the block form (22) may be permuted (for example) with the reverse Cuthill–McKee algorithm[47] to reduce the bandwidth before applying a linear solver in the Newton iteration. Figure 3 depicts the sparse, banded structure of the Jacobian over a second-order finite difference approximation to the system (18) on an $m \times m$ computational grid.

4.3 | Padé error analysis

For the functional Padé approximant to be effective, it must represent the flow solutions to a specified order of accuracy at ε values that lie outside the convergence region of the perturbation series. Part of the analysis to follow is to determine numerically the largest ε values in which the flow solutions can be accurately represented by the Padé approximants. Convergence results for functional Padé approximants require knowledge of the structure of the true flow solutions,[36] and thus the effective domain of convergence must be determined numerically. Ideally, the choice of the degree $M = 2k$ of the denominator polynomial agrees with the true number of poles of each respective flow solution in the ε-complex plane, which is generally unknown. In practical numerical applications, the best arrangement tends to be the diagonals of the Padé table, meaning $N = M$, or slightly off diagonal, where $M = N \pm 1$.[34,36,44]

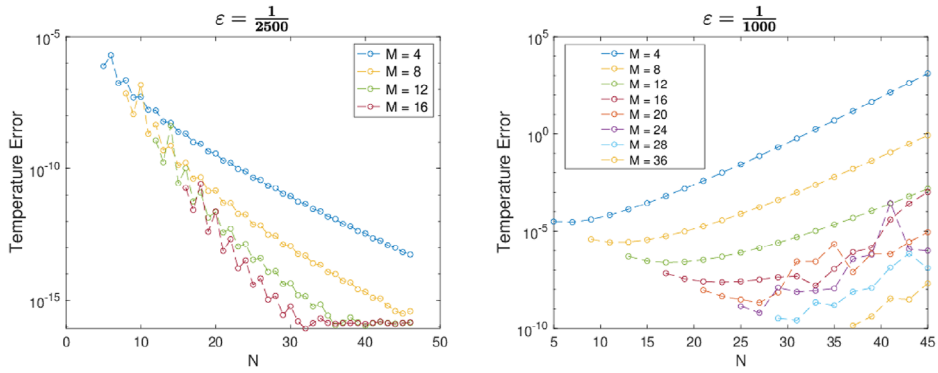

FIGURE 4 The forward error in the functional Padé approximant for temperature fluctuation is presented for two ε values across various N, M values. The left panel exhibits rapid convergence in N for every fixed M, while the right panel depicts lower error for N, M values near the diagonal of the Padé table.

Figure 4 depicts the forward error in the vector 2-norm of functional Padé approximants to the temperature fluctuations across various choices for N, M and for two separate ε values. Error is defined relative to true flow solutions obtained from the fixed-point method[19] or Newton's method (19) described in the previous subsection. The domain size of $L = 4$ remains fixed in all computational results. Based on the formulation of the functional Padé approximants, we require M to be even with the condition that $N \geq M - 1$. The parity restriction on M permits denominator polynomials with strictly nonreal roots, which is beneficial for computational purposes as we vary ε along the real line. The top panels depict error for an ε value within the perturbation series convergence region and the bottom panels depict error for ε at the edge of the convergence region for the fixed-point method described in Ref. [19].

Figure 4 depicts the convergence of the Padé approximant in N for a fixed M when ε is small and within the perturbation series convergence region. Since, however, the primary motivation to employ Padé approximants comes from its ability to represent functions well outside the domain of analyticity, particular attention is paid to the error for increasingly large ε values. When ε increases, the lowest error approximants tend to lie near the diagonal of the Padé table such that $M = N$ for even N and $M = N - 1$ for odd N (see the right panel of Figure 4).

5 | PADÉ POLE ANALYSIS

Since the steady flow solutions are represented with a rational function in the parameter ε, this functional Padé approximant can be used to estimate the locations of ε-singularities within the complex plane. From analyzing the convergence properties of the perturbation series representation of the steady flow solutions (2), one can estimate the domain of ε values in which the perturbation series converges. For the same simulation parameters in the previous section, we estimate $\varepsilon^* \approx \frac{1}{1850} = 5.4 \times 10^{-4}$ to be the effective radius of convergence. This radius can also be approximated using the roots of the denominator polynomial.

The zeros of the denominator polynomial of the functional Padé approximant represent a natural estimate of these singularities; however, their number and location depend on the degree of the denominator polynomial M. Since the distribution and number of poles is that which is to be determined, we search over the space of allowed M values to observe the behavior of the

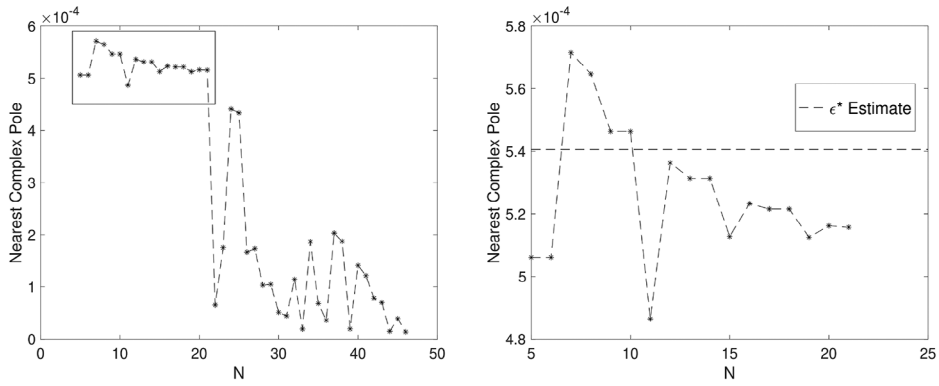

FIGURE 5 Left: The distance from the origin to the nearest pole in the complex plane for the functional Padé approximants across various N values is depicted. Right: The poles within the bounding box that surround the estimated radius of convergence of the perturbation series are plotted as a function of N. (2). The numerator degree approaches 21 before closer poles arise due to floating point errors. The radius of convergence estimate $\varepsilon^* = 5.4 \times 10^{-4}$ comes from the least squares estimate in Section 3 for $L = 4$.

denominator zeroes in the functional Padé approximant. Figure 5 depicts the closest ε-pole in the complex plane as a function of N with $M = N$ for even N and $M = N - 1$ for odd N. Only the nearest pole to the origin between T, ω, and ψ is shown, and poles at the origin corresponding to pole-zero pairs, or Froissart doublets,[39] are ignored. The nearest poles tend to approach a value close to the estimated radius of convergence as $N \to 21$, past which the pole locations become more erratic due to floating point errors arising from the increasing size of the perturbation terms. The right panel depicts the pole locations surrounding the estimated radius of convergence as N approaches 21.

We note that the $N = 25, M = 24$ is the highest order representation that contains no real poles, and thus allows arbitrarily large real ε. This behavior is desired in the high amplitude limit and should produce a useful initialization for the Newton method presented in Section 6.

5.1 | Comparison to classical Padé approximation

Instead of the functional Padé approximant treated presented above, one could instead calculate a classical Padé approximant to the pointwise discretization of the steady flow solutions. That is, for each point (x, y) in the 2D discretization of the steady flow solutions, a classical Padé approximant is constructed from the associated (x, y) points in the perturbation terms. For the temperature case, this is represented by

$$T(x, y; \varepsilon) \approx \frac{\sum_{n=0}^{N} \varepsilon^n A_n(x, y)}{\sum_{n=0}^{M} \varepsilon^n B_n(x, y)} = \frac{A_0(x, y) + \varepsilon A_1(x, y) + \cdots + \varepsilon^N A_N(x, y)}{B_0(x, y) + \varepsilon B_1(x, y) + \cdots + \varepsilon^M B_M(x, y)}. \tag{23}$$

The classical Padé numerator and denominator coefficients can be pointwise computed through any standard approach, yet it is useful to consider more robust approaches when the matrix $\mathcal{A}$ is singular or ill-conditioned, or if there is noise in the perturbation terms, possibly arising due to floating-point errors. Gonnet, Güttel, and Trefethen[39] introduce one such robust approach, which implements the normalization condition such that $\|\mathbf{B}\| = 1$, and determines the

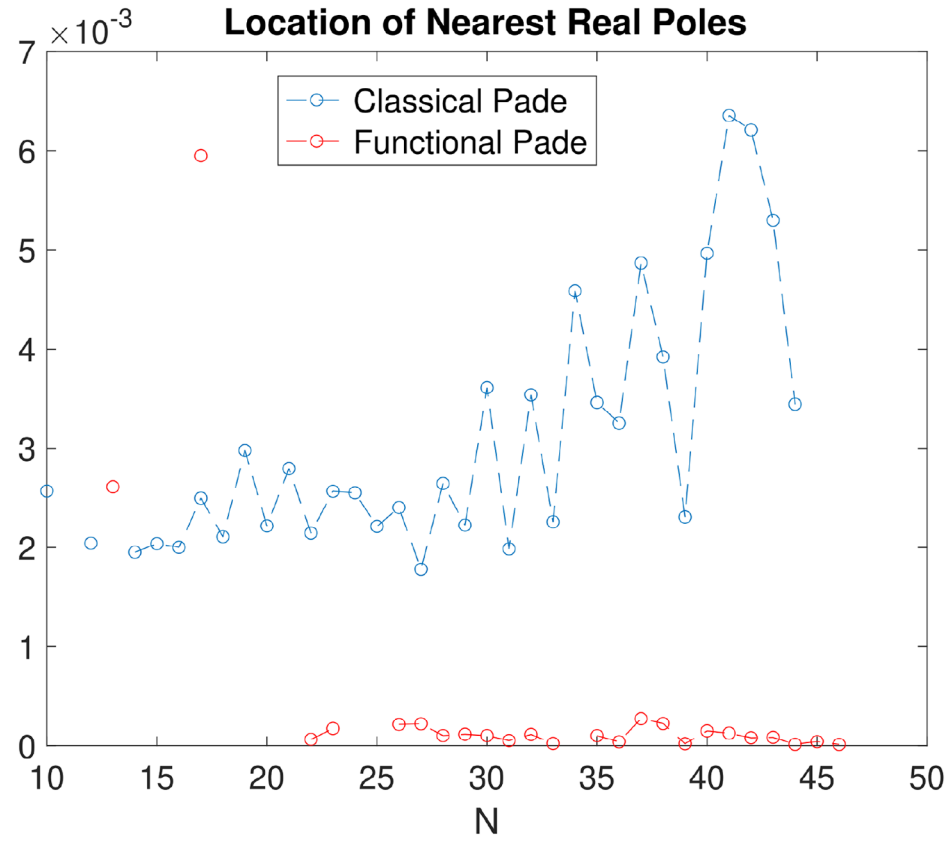

FIGURE 6 The distance from the origin to the nearest genuine real pole with classical and functional Padé approximation. Functional Padé approximation avoids real poles for most $N < 22$ before floating point errors dominate, while classical Padé approximation creates real poles for nearly all N values.

denominator coefficients with an SVD approach; similar to the method introduced for functional Padé approximation.

While this classical approach will ostensibly provide an improved $\mathcal{O}(\varepsilon^{N+M+1})$ accuracy compared to the functional Padé's $\mathcal{O}(\varepsilon^{N})$, this result must be held in consideration with the new pointwise ε-pole distribution. By defining unique denominator coefficients at each point in discretization of the steady flow solutions, we introduce M poles associated to each of the m^2 points in the discretization. If any of these poles lie on the real line, the loss of regularity in the classical Padé representation may result in a significant departure from the true steady flow solution. Figure 6 provides the nearest real pole distribution for classical and functional Padé approximation as N increases and $M = N - 1$ in the top panel.

Gonnet, Güttel, and Trefethen[39] introduce a coloring scheme for poles based on the complex residue (distance between a pole and the nearest zero). If a pole is very close to a zero, it is likely to be spurious and to not represent a genuine singularity in the function. For large residues, the pole is likely to be genuine. In between, there is some uncertainty in the degree to which a Padé pole represents a genuine singularity. The bottom panel of Figure 7 follows the same convention, denoting red poles as likely to be spurious, blue poles as likely to be genuine, and green poles as uncertain.

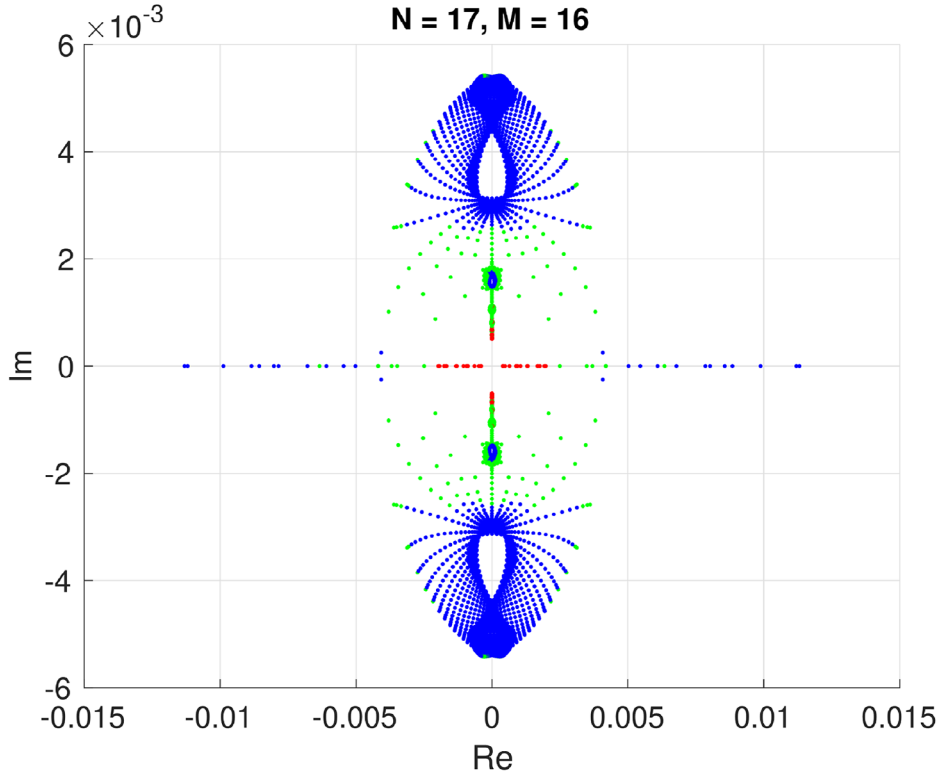

FIGURE 7 The pole distribution in the complex plane using an adaptation of the coloring scheme described in Ref. [39] for the determination of a genuine or spurious pole. The poles are colored based on the residue r such that red: $r < 10^{-10}$, green: $10^{-10} \leq r \leq 10^{-5}$, blue: $10^{-5} < r$.

The poles of the classic Padé approximate in Figure 7 include a sequence of real poles near the origin. The poles closest to the origin are classified as spurious, but as the residue grows along the real line the poles are eventually classified as genuine. Presently, there is a noted absence in the literature that aims to connect Padé approximation methods to modern algebraic geometry, with further discussion on Padé approximants on complex manifolds provided by Ref. [48]. Rather than rely on the classification scheme in Ref. [39] for the poles of classical Padé approximant, the functional Padé approximant can be used and these potentially spurious real poles can be avoided altogether. Therefore, the use of functional approximation is preferred for computing steady flow solutions in the large ε limit, even with the loss in asymptotic accuracy compared to classical pointwise Padé approximation. This functional Padé approximant is observed to have good qualitative agreement with the shape of steady flow solutions up to $\varepsilon \approx 0.05$ for the simulation parameters in Section 6. Figure 8 summarizes the four steady fluid solvers under consideration based on their computational cost and ε-range of computation.

6 | SIMULATIONS FOR LARGE ε

We now present results from applying the Newton iteration (21) with an initialization determined from the functional Padé approximants (10) for each of the steady flow solutions as ε becomes

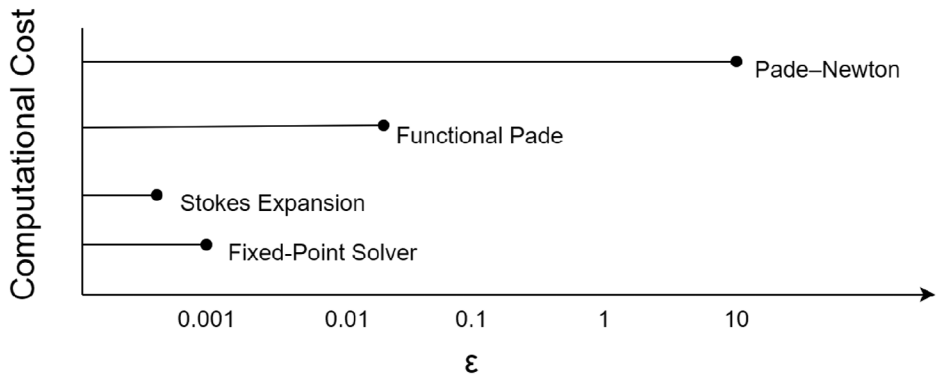

FIGURE 8 Four distinct steady fluid solvers are arranged top to bottom from most computationally expensive to least computationally expensive. The *x*-axis describes the range of intensity parameter ε for which each steady solver can resolve solutions. The Padé–Newton method offers a several orders of magnitude increase in computable ε forcing when compared to alternative methods.

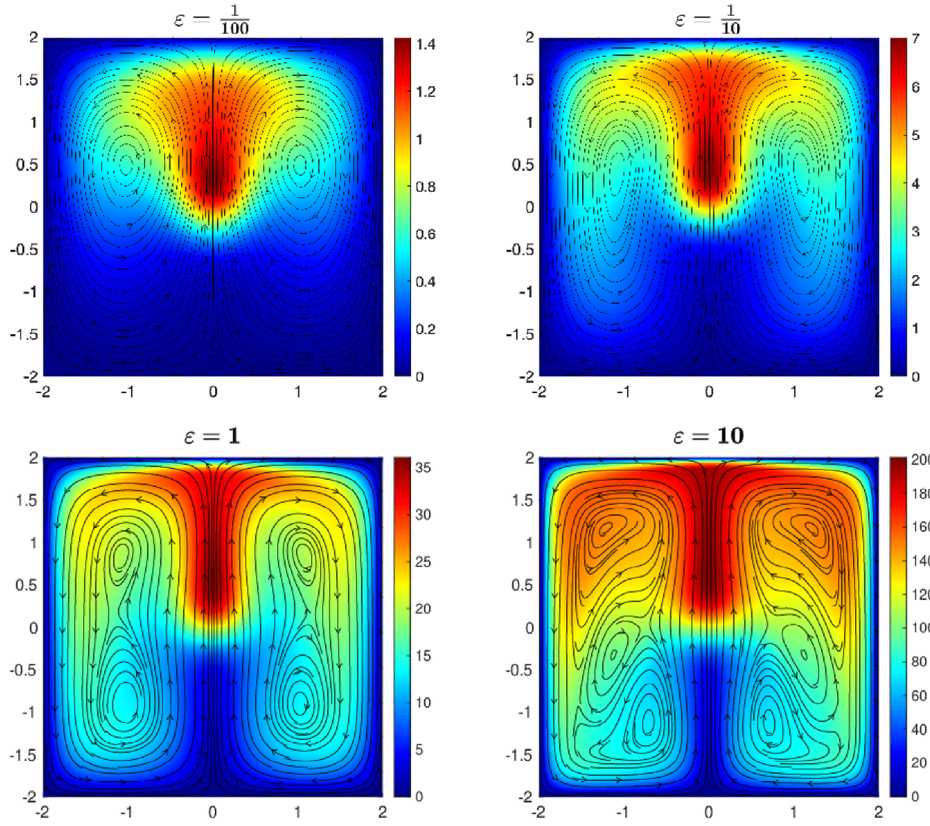

FIGURE 9 Each panel depicts the two-dimensional temperature fluctuation (in degrees K) and streamlines for $\varepsilon = \frac{1}{100}$, $\varepsilon = \frac{1}{10}$, $\varepsilon = 1$, and $\varepsilon = 10$. These steady solutions were computed via the Padé–Newton method.

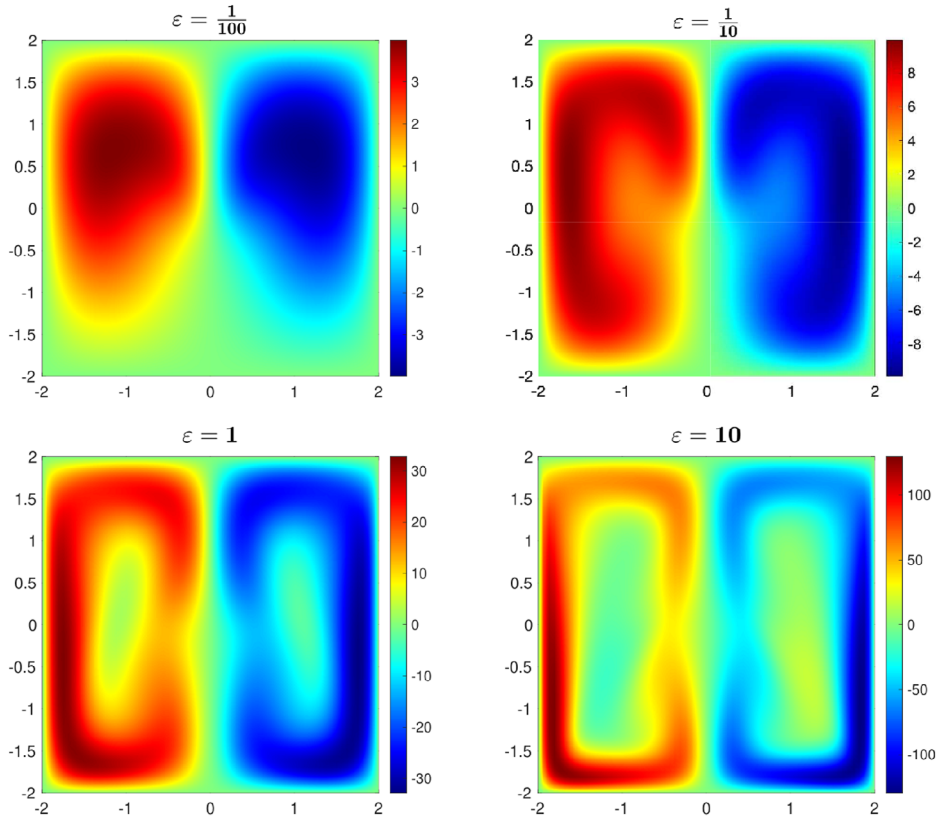

FIGURE 10 Each panel depicts the two-dimensional vorticity for $\varepsilon = \frac{1}{100}$, $\varepsilon = \frac{1}{10}$, $\varepsilon = 1$, and $\varepsilon = 10$. These steady solutions were computed via the Padé–Newton method.

large. We fix the simulation parameters to be the same from Section 3 and to represent air at standard laboratory conditions, with reference temperature $\tau_0 = 300$ K, convective length scale $w_0 = 1$ cm, domain length $L = 4$ cm, velocity scale $U = 1$ cm/s, and intrinsic flow parameters Re $= 6.67$, Pe $= 5$, Ri $= 981$. We choose $\varepsilon = 1$ to represent the high amplitude case. The functional Padé approximants use $N = 25$, $M = 24$.

The Newton iteration converges, and thus the functional Padé approximant provides a good initial guess for the steady flow solutions in the high amplitude regime. Figures 9 and 10 provide the temperature fluctuation, streamlines, and vorticity field as determined from the Newton iteration at four separate ε values.

We find that the Padé–Newton iteration allows for the simulation of ε values up to four orders of magnitude larger than the fixed-point method.[10,19] Vortex cores emerge in the flow as ε varies, where $\varepsilon = 0.2$ and $\varepsilon = 5$ represent critical values in which new stagnation points are created in the flow. For the laser applications that motivate this work, the large gradients in the flow near the boundary for $\varepsilon = 10$ are unexpected, which suggests that additional modeling of the temperature boundary condition would be of value.[9–11]

Although existence and uniqueness results exist for small ε,[19] the existence of other steady solutions for the Boussinesq equations for large intensity parameter is unknown. If there are additional steady solutions different from those found in Figures 9 and 10, then the choice of initialization may play a critical role in the convergence of the Newton method. Further, numerical continua-

tion methods may be applied to find steady solutions at even higher intensity forcing or to arrive at an alternate steady state from the one determined by the Padé–Newton method.

7 | CONCLUSIONS

The premise of this work was centered around the representation of steady solutions to the two-dimensional Boussinesq equations with internal forcing. The steady flow solutions are analytic in the intensity parameter ε, which produces a region of convergence through a Stokes expansion for small ε. In pursuit of finding steady solutions for larger ε values, functional Padé approximation was utilized to approximate the flow solutions over the two-dimensional domain. These representations proved useful for estimating the complex plane singularities in the true flow solutions, and can be used as a good approximation for moderate intensities outside the domain of convergence of the Stokes expansion. For larger ε values, the functional Padé approximant can be used as an initialization to a Newton iteration. The advantages of this hybrid approach include the ability to store Padé coefficients for a given fluid domain and the acceleration of converge of the Newton solver, as compared to modern numerical continuation techniques. With the establishment of this Padé–Newton method, one can, for example, use the high-intensity flow solutions in simulations of paraxial laser propagation.[9,10] Future research efforts should focus on the determination of proper boundary conditions, the validity of the Boussinesq model at high forcing intensities,[49] the relationship of flow properties with domain size, and the existence and computation of alternative steady-state flow solutions.

CONFLICT OF INTEREST STATEMENT

The authors declare no conflicts of interest.

DATA AVAILABILITY STATEMENT

Data sharing is not applicable to this article as no data sets were generated or analyzed during this study.

ORCID

Jeremiah S. Lane https://orcid.org/0000-0001-9159-1819

REFERENCES

1. Pilkington A, Rosic B, Tanimoto K, Horie S. Prediction of natural convection heat transfer in gas turbines. *Int J Heat Mass Transfer*. 2019;141:233-244, doi:10.1016/j.ijheatmasstransfer.2019.06.074
2. Abdillah H, Saputra G, Novitrian, Permana S. *Study of Natural Convection Passive Cooling System for Nuclear Reactors*. Vol 877. Institute of Physics Publishing; 2017.
3. Vela E, Hafez M, Régnier S. Laser-induced thermocapillary convection for mesoscale manipulation. *Int J Optomechatronics*. 2009;3:289-302, doi:10.1080/15599610903389477
4. Flores-Flores E, Torres-Hurtado SA, Páez R, et al. Trapping and manipulation of microparticles using laser-induced convection currents and photophoresis. *Biomed Opt Express*. 2015;6:4079, doi:10.1364/boe.6.004079
5. Mourad A, Aissa A, Mebarek-Oudina F, et al. Galerkin finite element analysis of thermal aspects of Fe3O4-MWCNT/water hybrid nanofluid filled in wavy enclosure with uniform magnetic field effect. *Int Commun Heat Mass Transfer*. 2021;126:105461, doi:10.1016/j.icheatmasstransfer.2021.105461
6. Jamshed W, S SUD, Goodarzi M, et al. Evaluating the unsteady Casson nanofluid over a stretching sheet with solar thermal radiation: an optimal case study. *Case Stud Therm Eng*. 2021;26:101160, doi:10.1016/j.csite.2021.101160

7. Nong H, Fatah AM, Shehzad SA, Ambreen T, Selim MM, Albadarin AB. Numerical modeling for steady-state nanofluid free convection involving radiation through a wavy cavity with Lorentz forces. *J Mol Liq*. 2021;336, doi:10.1016/j.molliq.2021.116324
8. Putra N, Roetzel W, Das SK. Natural convection of nano-fluids. *Heat Mass Transf./Waerme- und Stoffuebertragung*. 2003;39:775-784, doi:10.1007/s00231-002-0382-z
9. Akers BF, Reeger JA. Numerical simulation of thermal blooming with laser-induced convection. *J Electromagn Waves Appl*. 2019;33:96-106, doi:10.1080/09205071.2018.1528183
10. Lane JS, Cook J, Richardson M, Akers BF. Numerical simulation of steady-state thermal blooming with natural convection. *Appl Opt*. 2023;62:2092. doi:10.1364/AO.484224
11. Akers BF, Fiorino ST, Reeger JA. Thermal blooming with laser-induced convection: radial basis function simulation. *Appl Opt*. 2023;62:G77-G84.
12. Tritton DJ. *Physical Fluid Dynamics*. Springer; 1977.
13. Pandey S, Park YG, Ha MY. An exhaustive review of studies on natural convection in enclosures with and without internal bodies of various shapes. *Int J Heat Mass Transfer*. 2019;138:762-795, doi:10.1016/j.ijheatmasstransfer.2019.04.097
14. Miroshnichenko IV, Sheremet MA. Turbulent natural convection heat transfer in rectangular enclosures using experimental and numerical approaches: a review. *Renew Sustain Energy Rev*. 2018;82(Pt 1):40-59. doi:10.1016/j.rser.2017.09.005
15. Choi S-K, Kim S-O. Turbulence modeling of natural convection in enclosures: a review. *J Mech Sci Technol*. 2012;26. doi:10.1007/s12206-011-1037-0
16. Coffin P, Maute K. A level-set method for steady-state and transient natural convection problems. *Struct Multidiscip Optim*. 2016;53:1047-1067, doi:10.1007/s00158-015-1377-y
17. Hussein AK, Hussain SH. *Numerical Analysis of Steady Natural Convection of Water in Inclined Square Enclosure with Internal Heat Generation*. IEEE; 2010.
18. Öztop HF, Estellé P, Yan WM, Al-Salem K, Orfi J, Mahian O. A brief review of natural convection in enclosures under localized heating with and without nanofluids. *Int Commun Heat Mass Transfer*. 2015;60:37-44, doi:10.1016/j.icheatmasstransfer.2014.11.001
19. Lane JS, Akers BF. Two-dimensional steady Boussinesq convection: existence, computation and scaling. *Fluids*. 2021;6, doi:10.3390/fluids6120425
20. Haajizadeh M, Ozguc AF, Tien CL. Natural convection in a vertical porous enclosure with internal heat generation. *Int J Heat Mass Transfer*. 1984;27(10):1893-1902, doi:10.1016/0017-9310(84)90171-6
21. Nicholls DP, Reitich F. A new approach to analyticity of Dirichlet-Neumann operators. *Proc R Soc Edinb A: Math*. 2001;131(6):1411-1433.
22. Nicholls DP, Reitich F. Stability of high-order perturbative methods for the computation of Dirichlet–Neumann operators. *J Comput Phys*. 2001;170(1):276-298.
23. Nicholls DP, Reitich F. Stable, high-order computation of traveling water waves in three dimensions. *Eur J Mech B Fluids*. 2006;25(4):406-424.
24. Akers B, Nicholls DP. Wilton ripples in weakly nonlinear dispersive models of water waves: existence and analyticity of solution branches. *Water Waves*. 2021;3:25-47, doi:10.1007/s42286-020-00034-w
25. Akers BF, Gao W. Wilton ripples in weakly nonlinear model equations. *Commun Math Sci*. 2012;10(3):1015-1024.
26. Creedon R, Deconinck B, Trichtchenko O. High-frequency instabilities of the Kawahara equation: a perturbative approach. *SIAM J Appl Dyn Syst*. 2021;20(3):1571-1595.
27. Nicholls DP. Boundary perturbation methods for water waves. *GAMM-Mitteilungen*. 2007;30:44-74, doi:10.1002/gamm.200790009
28. Nicholls DP. Method of field expansions for vector electromagnetic scattering by layered periodic crossed gratings. *J Opt Soc Am A*. 2015;32:701, doi:10.1364/josaa.32.000701
29. Akers B, Nicholls DP. Spectral stability of deep two-dimensional gravity water waves: repeated eigenvalues. *SIAM J Appl Math*. 2012;72(2):689-711.
30. Akers B. Spectral stability of deep two-dimensional gravity-capillary water waves. *Stud Appl Math*. 2013;130(2):81-107.
31. Akers B, Nicholls DP. The spectrum of finite depth water waves. *Eur J Mech B Fluids*. 2014;46:181-189.

32. Nicholls DP. Spectral stability of traveling water waves: analytic dependence of the spectrum. *J Nonlinear Sci*. 2007;17:369-397.
33. Creedon RP, Deconinck B, Trichtchenko O. High-frequency instabilities of Stokes waves. *J Fluid Mech*. 2022;937:A24.
34. Baker GA, Graves-Morris P. *Pade Approximants Part I: Basic Theory*. Addison-Wesley Publishing Company; 1981.
35. Baker GA, Graves-Morris P. *Padé Approximants*. 2nd ed. Cambridge University Press; 1996.
36. Graves-Morris PR, Iseghem JV. Row convergence theorems for vector-valued Padé approximants. *J Approx Theory*. 1997;90:153-173, doi:10.1006/jath.1996.3077
37. Graves-Morris PR, Roberts DE. Problems and progress in vector Padé approximation. *J Comput Appl Math*. 1997;77:173-200.
38. Nicholls DP, Reitich F. Stable, high-order computation of traveling water waves in three dimensions. *Eur J Mech A Solids*. 2006;25:406-424, doi:10.1016/j.euromechflu.2005.11.003
39. Gonnet P, Güttel S, Trefethen LN. Robust Padé Approximation via SVD. *SIAM Rev*. 2013;55(1):101-117.
40. Gilewicz J, Kryakin Y. Froissart doublets in Padé approximation in the case of polynomial noise. *J Comput Appl Math*. 2003;153:235-242, doi:10.1016/S0377-0427(02)00674-X
41. Evans LC. *Partial Differential Equations*. 2nd ed. Department of Mathematics, University of California, Berkeley, American Mathematical Society. 2010. doi:10.1090/gsm/019
42. Brezis H. *Functional Analysis, Sobolev Spaces, and Partial Differential Equations*. Springer; 2010.
43. Sprangle P, Peñano JR, Ting A, Hafizi B. Propagation of high-energy lasers in a maritime atmosphere. *NRL Review*. 2004:59-65.
44. Bender CM, Orszag SA. *Advanced Mathematical Methods for Scientists and Engineers: Asymptotic Methods and Perturbation Theory*. 2nd ed. Springer-Verlag Inc.; 1999.
45. Thukral R. A family of Padé-type approximants for accelerating the convergence of sequences. *J Comput Appl Math*. 1999;102(2):287-302. doi:10.1016/S0377-0427(98)00229-5
46. Baker GA. Defects and the Convergence of Padé Approximants. *Acta Appl Math*. 2000;61:37-52. doi:10.1023/A:1006467728464
47. Gibbs NE, Poole WG, Stockmeyer PK. An Algorithm for Reducing the Bandwidth and Profile of a Sparse Matrix. *SIAM J Numer Anal*. 1976;13(2):236-250.
48. Bertola M. *Padé Approximants on Riemann Surfaces and KP Tau Functions*. Vol 11. Springer International Publishing; 2021.
49. Mayeli P, Sheard GJ. Buoyancy-driven flows beyond the Boussinesq approximation: a brief review. *Int Commun Heat Mass Transfer*. 2021;125, doi:10.1016/j.icheatmasstransfer.2021.105316

How to cite this article: Lane JS, Akers BF. Steady Boussinesq convection: Parametric analyticity and computation. *Stud Appl Math*. 2024;e12740. https://doi.org/10.1111/sapm.12740